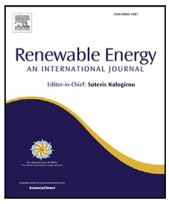
Renewable Energy 245 (2025) 122784



Contents lists available at ScienceDirect

Renewable Energy

journal homepage: www.elsevier.com/locate/renene





Impact of porous host materials on the compromise of thermochemical energy storage performance

Jianbin Chen, Yong Zhang *, Ziwei Chen, Guohui Gan, Yuehong Su *

Department of Architecture and Built Environment, Faculty of Engineering, University of Nottingham, NG7 2RD, United Kingdom

ARTICLE INFO

Keywords:
Thermochemical energy storage
Thermochemical materials
Reaction rate
Volumetric salt content
Energy storage density

ABSTRACT

Thermochemical energy storage (TCES) systems address renewable energy intermittency with high energy density and negligible heat loss. $CaCl_2$, known for its high reaction enthalpy and cost-effectiveness, faces challenges such as deliquescence and poor mass transfer. Incorporating porous host materials mitigates these issues. This study examines the impact of pore structure on TCES performance at both particle and reactor scales, utilizing five porous composites prepared via vacuum impregnation with vermiculite (V), expanded perlite (EP), pumice (Pm), silica gel (SG), and zeolite 13x (Z) as host materials. At the particle scale, macroporous composites (V-$CaCl_2$, EP-$CaCl_2$) achieved high gravimetric salt contents (>65%) and moderate volumetric energy density (0.55–0.65 GJ/m^3) but exhibited slower reaction kinetics. Mesoporous SG-$CaCl_2$ composite exhibited superior reaction rates and equilibrium hydration capacity, achieving sustained high-temperature output with an average temperature rise of 16.01 °C under RH=50%, albeit with a significant pressure drop across a 5 cm thick reaction bed, with a 0.2 m/s cross-sectional air velocity (101.06 Pa). EP-$CaCl_2$ provided a balance of smooth heat release, low resistance (6.88 Pa), and favorable volumetric energy density (0.65 GJ/m^3). These findings underline the necessity of selecting appropriate porous host materials to optimize specific performance metrics such as energy density, reaction kinetics, and system-level thermal output characteristics, providing a pathway for designing more efficient and application-specific TCES systems.

1. Introduction

Renewable energy has achieved significant advancements worldwide, with numerous countries making substantial investments in solar, wind, and other sustainable energy sources [1]. However, the intermittent nature of these systems presents challenges to grid stability, emphasizing the critical need for effective energy storage solutions. Globally, the building sector accounts for approximately 30% of total energy consumption, with nearly half of this energy dedicated to space and water heating needs [2]. As nations strive toward low-carbon energy futures, the demand for sustainable heating solutions becomes increasingly critical. Thermochemical energy storage (TCES) stands out due to its high energy density (0.5–3 GJ/m^3 [3]), long-term stability, and near-zero heat loss [4], making it suitable for both compact and seasonal applications. By efficiently capturing and storing industrial waste heat or solar energy, TCES plays a pivotal role in advancing global efforts to develop low-carbon heating solutions [5–8].

Among various TCES materials, hydrated salts are widely used for low-temperature applications due to their suitable operating temperature range, low regeneration temperature (<150 °C), ease of reaction with water vapor, non-toxic nature, and cost-effectiveness [9,10]. Pure salts are highly attractive for compact TCES systems because of their high volumetric energy storage density [11,12]. However, despite their advantages, the application of pure salts in TCES systems presents several challenges. During the discharging process, if the ambient humidity exceeds the salt's deliquescence relative humidity (DRH), the salt can absorb excessive moisture and dissolve into solution, forming a liquid film that inhibits the hydration reaction and raises corrosion concerns when dripping onto reactor surfaces [13,14]. Similarly, during the charging process, the low melting points of the highest hydrates of some salts can pose challenges. If the temperature is not properly controlled, melting may occur. For example, $SrCl_2 \cdot 6H_2O$ decomposes into a solution and dihydrate when the charging temperature exceeds 61.3 °C [15,16], $CaCl_2 \cdot 6H_2O$ begins to decompose into $CaCl_2 \cdot 4H_2O$ and a solution at 30.1 °C [17]. In addition, pure salts are prone to agglomeration during cycling, which diminishes performance over time [18]. Furthermore, the low mass transfer performance of pure salts limits their reaction kinetics, particularly in large-scale systems.

To mitigate the challenges associated with the standalone use of hydrated salts, researchers have explored incorporating porous host materials to disperse the salts. This approach involves impregnating

* Corresponding authors.
E-mail addresses: yong.zhang@nottingham.ac.uk (Y. Zhang), yuehong.su@nottingham.ac.uk (Y. Su).

https://doi.org/10.1016/j.renene.2025.122784
Received 30 November 2024; Received in revised form 28 January 2025; Accepted 28 February 2025
Available online 10 March 2025
0960-1481/© 2025 The Authors. Published by Elsevier Ltd. This is an open access article under the CC BY license (http://creativecommons.org/licenses/by/4.0/).

salt solutions into porous materials to form composites 'salt inside porous matrix' (CSPM) [19]. The benefits are significant: (1) porous materials typically have a large specific surface area (e.g., silica gel with >400 m^2/g [20], and zeolite 13x with >500 m^2/g [21]), allowing salts to be distributed over the surface, thereby increasing the reactive contact area and enhancing mass transfer efficiency; (2) the pore structure provides capillary action to accommodate solutions, reducing the inhibitory effect of liquid film formation caused by deliquescence or melting during hydration and dehydration processes [22]; (3) some porous materials, such as expanded graphite with a thermal conductivity of approximately 200 W/m·K [23], enhance heat transfer properties and further stabilize reaction dynamics. By physically confining salts within their pores, porous host materials mitigate agglomeration issues, improve cycling performance, and expand the applicability of salts with lower deliquescence relative humidity.

The integration of porous host materials not only improves the performance of traditional hydrated salts but also broadens the range of applicable salts by enabling the use of those with lower DRH and favorable reaction kinetics (e.g., $CaCl_2$ [24]). Common porous host materials include activated carbon [25], alumina [26], bentonite [26], silica gel [20], zeolite 13x [17,21], expanded graphite [27], expanded perlite [28,29], and vermiculite [30]. Additionally, metal–organic frameworks (MOFs) have been explored for their high surface area and tunable pore structures [25]. However, their high production costs remain a barrier to large-scale applications.

While the incorporation of porous host materials enhances reaction stability and compatibility, it reduces the volumetric energy storage density (ESD_v) from the theoretical 1.3 GJ/m^3 to 0.3–0.65 GJ/m^3 [31]. To overcome this limitation, optimizing impregnation techniques has become a strategy for enhancing salt loading. Methods such as multiple impregnation [32], vacuum impregnation [33,34], and high-concentration impregnation [35] have shown significant potential in increasing salt content. For instance, vacuum impregnation applied to vermiculite has demonstrated the ability to enhance volumetric energy density by up to 1.5 times compared to conventional techniques [36]. This improvement is attributed to vacuum impregnation's capacity to drive the solution deeper into the porous structure, enabling more effective utilization of the pore volume and substantially boosting the porous materials' salt-loading capability. However, the benefits of high salt loading often come at the cost of pore blockage, which compromises reaction kinetics by hindering the transport of reactants [37–40]. On the other hand, the porosity and pore architecture of porous materials directly effect salt content, reaction kinetics, and the stability of composites during repeated cycles [41].

While particle-level experiments provide valuable insights into sorption characteristics, they often fail to capture the full spectrum of performance in packed beds. For instance, particle-level studies typically overlook critical reactor-level parameters, such as the void ratio within packed beds, the effective volumetric energy storage density, and the dynamic heat release characteristics. These aspects are crucial for practical applications but remain underexplored in previous studies focused solely on particle-scale behavior.

To bridge this knowledge gap, this study investigates the effect of pore structures in porous host materials on the charging and discharging performance of composites under high salt loading conditions. $CaCl_2$ was selected as the energy storage salt due to its cost-effectiveness, high reaction enthalpy, and compatibility with a range of porous host materials. This study goes beyond material-level synthesis and static adsorption behavior by integrating material- and reactor-level analyses to evaluate dynamic performance metrics, including water uptake, heat release, and pressure drop. By systematically examining composites with varying pore structures and size distributions, it provides insights into their reaction kinetics and scalability in packed bed systems under realistic operating conditions. These findings contribute to optimizing porous host materials for thermochemical energy storage systems, paving the way for more efficient and reliable solutions.

2. Experiment

2.1. Synthesis of composite

To investigate the effect of different pore structures on the performance of porous composites in the TCES system, five commonly used porous host materials were selected: macroporous vermiculite (V) and expanded perlite (EP), both sourced from UKGROW LTD; pumice (Pm) from Sigma-Aldrich; mesoporous silica gel (SG) from Strem Chemical, Inc.; and microporous zeolite 13x (Z) also from Strem Chemical, Inc.

The synthesis process, depicted in Fig. 1, consisted of four main stages: materials pre-treatment, vacuum impregnation, centrifugal draining, and oven drying. Vacuum impregnation was utilized to introduce the $CaCl_2$ solution into the porous host materials, with the goal of maximizing the salt content in the porous composites.

The pre-treatment stage involved sieving the mineral materials (V, EP, and Pm) through a 2.5 mm mesh to remove finer particles, washing them thoroughly with water to eliminate surface impurities, and drying them at 150 °C for 24 h. In contrast, SG and Z were dried at a higher temperature of 250 °C to ensure complete moisture removal. Simultaneously, $CaCl_2$ granules were dissolved in deionized water to prepare a 43% saturated solution. During the vacuum impregnation stage, the prepared solution was poured over the porous host materials in a beaker placed in a vacuum chamber, where the chamber pressure was reduced to 0.05 atm using a vacuum pump, held for 10 minutes, and then gradually restored to atmospheric pressure. The selection of this duration was based on preliminary experiments, which showed that extending the vacuum impregnation time beyond 10 minutes resulted in negligible improvement in salt loading. Excess solution was removed during the centrifugal draining stage by spinning the composites at 150 rpm for 1 minute to minimize surface salt retention. Finally, in the oven drying stage, the composites were dried at 150 °C for 24 h to remove residual moisture and stabilize their structure. Although single-layer materials could dry within 3–5 h, a 24-hour drying period was chosen to ensure complete dehydration when materials were stacked. The resulting composites were labeled based on their respective porous host materials: V-$CaCl_2$ for vermiculite-based composite, EP-$CaCl_2$ for expanded perlite-based composite, Pm-$CaCl_2$ for pumice-based composite, SG-$CaCl_2$ for silica gel-based composite, and Z-$CaCl_2$ for zeolite 13x-based composite.

The appearances of these raw porous host materials and their corresponding synthesized composites are shown in Fig. 2.

To comprehensively characterize the synthesized composites, a variety of techniques and instruments were employed to analyze their physical properties, chemical composition, and performance under static, dynamic, and desorption experimental conditions. Table 1 provides an overview of the key methods and instruments utilized in this study.

2.2. Physical parameter measurements

As illustrated in Fig. 3, the relationships between skeletal density ($\rho_{skeletal}$), particle density ($\rho_{particle}$), and bulk density (ρ_{bulk}) are crucial for evaluating volumetric energy storage density. Skeletal density refers to the density of the solid framework excluding pore spaces, while particle density includes internal pores. Bulk density represents the total mass per unit volume, including inter-particle voids [42].

Porosity (ε_{pore}), defined as the ratio of internal pore volume to particle volume, is a critical factor influencing the salt storage capacity of porous materials. While higher porosity enables greater salt loading, it may also reduce thermal conductivity and surface area.

The void ratio (ε_{void}), defined as the ratio of inter-particle voids to total bulk volume, is influenced by multiple factors, including particle shape, size distribution, and packing structure. Uniformly shaped particles and specific size distributions can reduce the void ratio by promoting tighter packing, while irregular shapes or broader size distributions may have varying effects depending on the interplay of

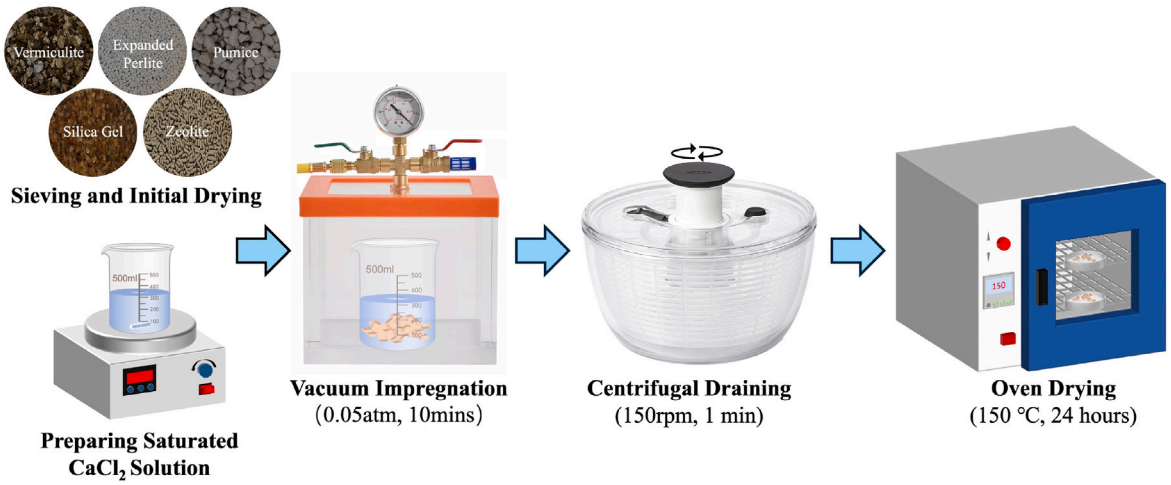


Fig. 1. Synthesis process of different porous composites.

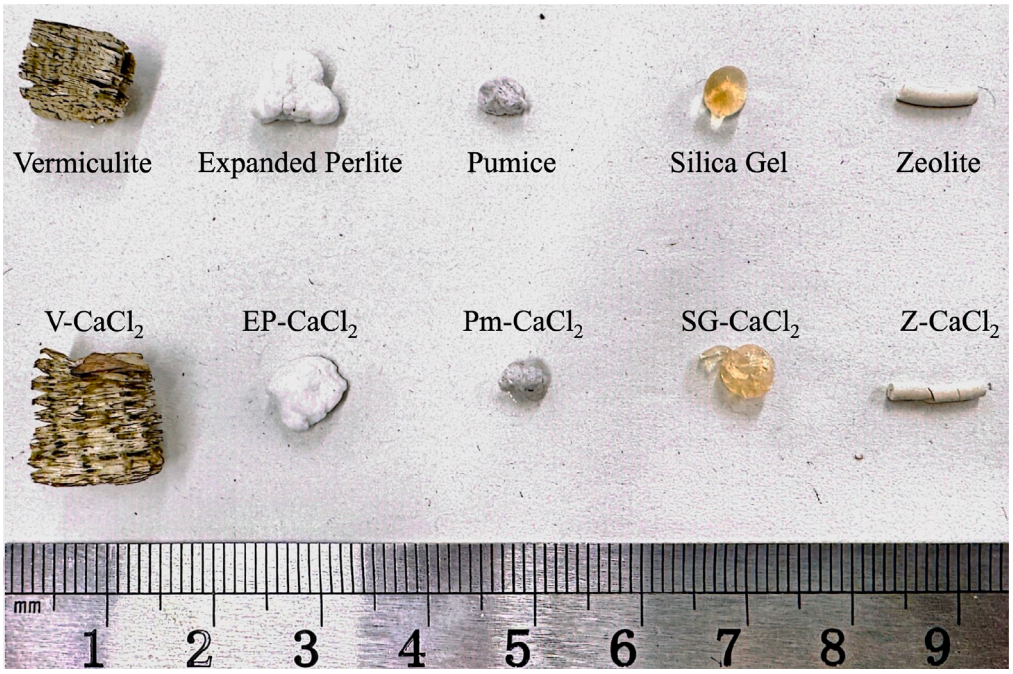


Fig. 2. Appearance of porous host materials (top row) and the corresponding synthesized composites (bottom row).

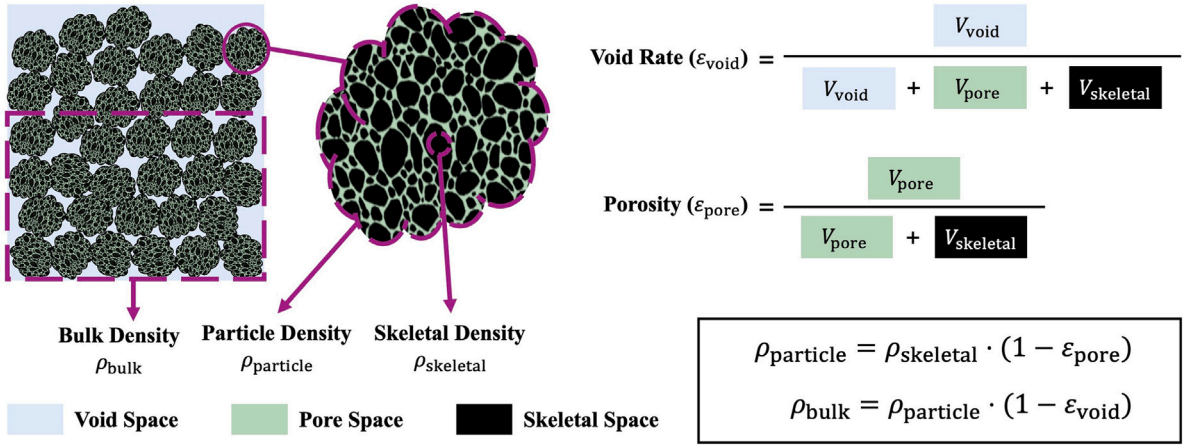


Fig. 3. Relationships among skeletal density, particle density, bulk density, porosity, and void ratio.

Table 1
Techniques and instruments used in characterization.

Category	Feature	Technique and instrument
General properties	Dimensions	Direct Measurement (Vernier Caliper)
	Bulk density (ρ_{bulk})	Volume and Mass Measurement
	Morphology	SEM Imaging (JEOL JSM-6490LV)
	Elemental composition	EDX (Oxford Instruments)
	Salt content (ϕ)	ICP-OES (Thermo Fisher iCAP PRO)
Microporous/Mesoporous materials	Skeletal density ($\rho_{skeletal}$)	Helium Pycnometry (Micromeritics AccuPyc II 1340)
	Specific surface area (SSA_g)	BET (Micromeritics ASAP 2460)
	Pore size distribution	BET (Micromeritics ASAP 2460)
	Pore volume	BET (Micromeritics ASAP 2460)
Macroporous materials	Skeletal density ($\rho_{skeletal}$)	MIP (Micromeritics AutoPore IV)
	Particle density ($\rho_{particle}$)	MIP (Micromeritics AutoPore IV)
	Specific surface area (SSA_g)	MIP (Micromeritics AutoPore IV)
	Pore size distribution	MIP (Micromeritics AutoPore IV)
	Pore volume	MIP (Micromeritics AutoPore IV)
Static sorption experiment	Water uptake (w)	Gravimetric Analysis (High-precision balance)
Dynamic sorption experiment	Pressure drop	Differential Pressure Sensor (Siemens QBM2030-30)
	Airflow velocity	Impeller Anemometer (ATP ET-965)
Desorption experiment	Residual water uptake (w)	Gravimetric Analysis (High-precision balance)
	Thermal and calorimetric properties	TGA/DSC (SDT650)

packing dynamics. A higher void ratio can enhance permeability but may compromise overall energy storage density.

At the bulk level, bulk density was measured using a graduated cylinder. At the particle level, dimensions were determined with a vernier caliper. Pore structure characteristics and elemental distributions were simultaneously analyzed using Scanning Electron Microscopy coupled with Energy Dispersive X-ray Spectroscopy (SEM-EDX, JEOL JSM-6490LV and Oxford Instruments), providing a comprehensive assessment of both morphological and compositional properties. The salt content in the composites was quantified by determining calcium concentrations with Inductively Coupled Plasma Optical Emission Spectrometry (ICP-OES, Thermo Fisher iCAP PRO).

Microporous and mesoporous materials were characterized for their specific surface area and pore volume using the Brunauer–Emmett–Teller (BET) method, carried out with a Micromeritics ASAP 2460 Surface Area Analyzer. Skeletal density was measured using a helium pycnometer (AccuPyc II 1340, Micromeritics). Porosity was calculated using the following equation:

$$\varepsilon_{pore} = \frac{V_{pore} \cdot \rho_{skeletal}}{1 + V_{pore} \cdot \rho_{skeletal}} \tag{1}$$

Here, V_{pore} represents the pore volume per unit mass (cm^3/g), and $\rho_{skeletal}$ denotes the skeletal density (g/cm^3).

For macroporous materials, Mercury Intrusion Porosimetry (MIP) was conducted using a Micromeritics AutoPore IV Porosimeter to obtain detailed data on pore volume, pore size distribution, and skeletal density.

2.3. Static sorption experiment

To evaluate the sorption capacity and reaction rates of composites under specific humidity conditions, 40 ml samples of porous composites were tested in a static sorption setup (Fig. 4). The experiments were carried out in a temperature-controlled chamber (Genlab Multi-Purpose Benchtop Incubator) at relative humidity (RH) levels of 33% and 53%. The humidity levels were maintained using supersaturated magnesium chloride and magnesium nitrate solutions, following Greenspan's methodology [43].

A shielding device was employed during sample placement to prevent unintended water uptake, ensuring chamber conditions stabilized before the start of measurements. To maintain uniform RH distribution, the salt solutions were agitated with a magnetic stirrer to minimize concentration stratification, while a fan facilitated moisture equilibrium and ensured consistent temperature and humidity throughout the chamber. Dual temperature and humidity sensors continuously monitored the internal conditions, and weight changes were recorded with a high-precision electronic balance connected to a data logging system at a sampling frequency of 1 Hz.

Water uptake (w) was expressed as water sorption per unit reactor volume (g/ml) to allow for better comparability among samples, as this method eliminates the influence of differences in particle density. The hydration ratio (χ), representing the moles of water absorbed per mole of $CaCl_2$ (mol/mol), was calculated using the following equation:

$$\chi = \frac{n_{H_2O}}{n_{CaCl_2}} = \frac{\frac{m(t)-m(t_0)}{M_{H_2O}}}{\frac{m(t_0)\phi}{M_{CaCl_2}}} \tag{2}$$

where n_{H_2O} and n_{CaCl_2} represent the moles of water and zeolite 13x (mol), $m(t)$ is the sample mass at time t (g), $m(t_0)$ is the initial mass of the sample (g), M_{H_2O} and M_{CaCl_2} are the molar masses of water and $CaCl_2$ (18.01 g/mol and 110.98 g/mol, respectively), and ϕ represents the salt content expressed as a percentage (%).

To analyze the sorption kinetics, the water uptake data were fitted using a first-order kinetic equation. This approach enabled the determination of the reaction rate constant k (h^{-1}) and the equilibrium water uptake w_e (g/ml):

$$\frac{dw(t)}{dt} = k(w_e - w(t)) \tag{3}$$

where $w(t)$ is the water uptake per unit volume at time t (g/ml).

2.4. Dynamic sorption experiment

Static sorption experiments provide valuable insights into equilibrium water uptake and reaction rates; however, their flat-layer sample arrangement fails to replicate the operational conditions of stacked configurations. In reactor-level applications, it is crucial to account for the packing voids between particles and the pressure drop across the packed bed, as these factors influence the volumetric energy storage density and the power required for system operation. Moreover, gas flow and changes in the contact surface area caused by the stacking state can substantially alter reaction kinetics. Dynamic sorption experiments not only effectively supplement these key characteristic insights but also enable macroscopic evaluation of the heat release properties of porous composites, which is critical for scenario-driven system design. Fig. 5 illustrates the experimental setup.

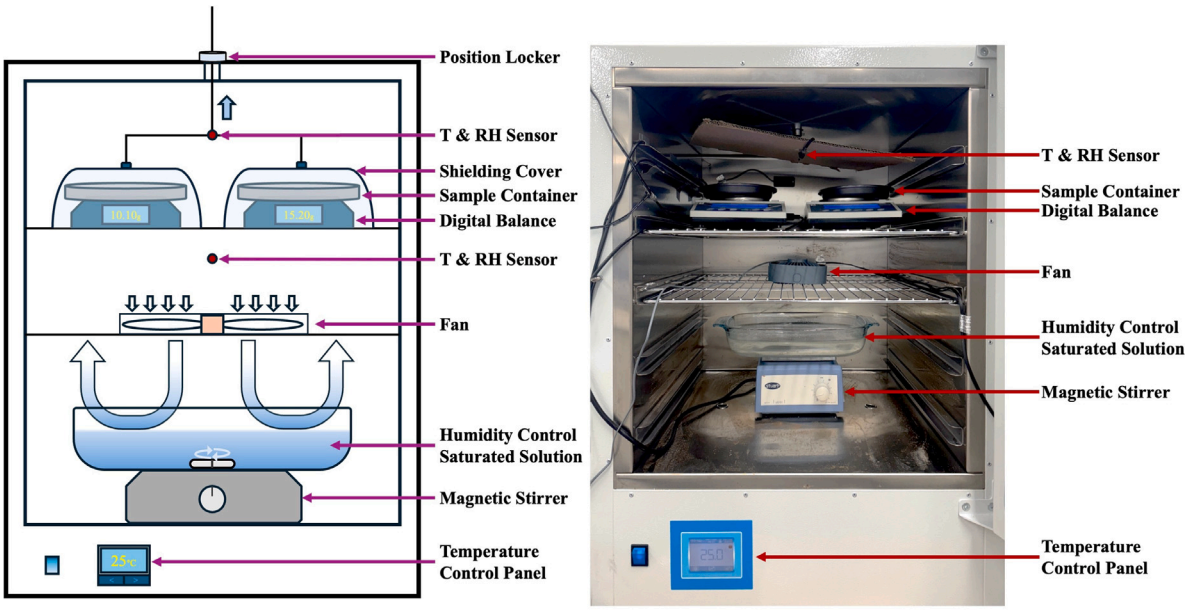


Fig. 4. Experimental setup for static sorption performance setup performance analysis.

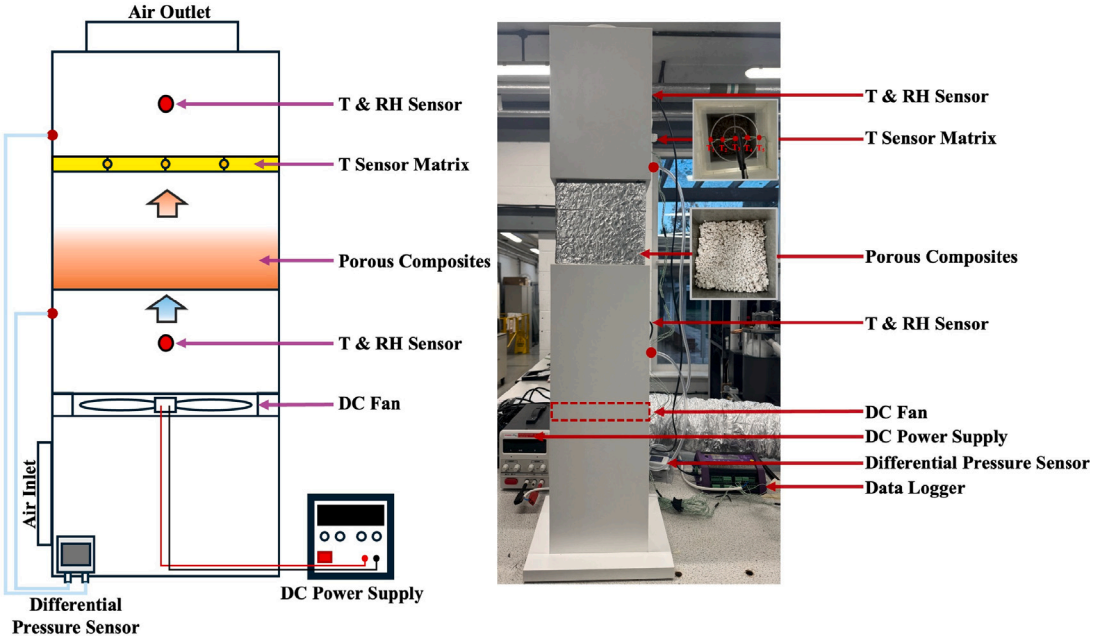


Fig. 5. The dynamic sorption experimental setup.

The inlet conditions were precisely controlled within a climate chamber. The airflow velocity in the reaction bed was adjusted and stabilized at 0.2 m/s using a DC adjustable power supply, with the voltage fine-tuned based on real-time measurements from an anemometer placed at the outlet. To monitor the pressure drop across the packed bed, differential pressure sensors were installed at the bed's inlet and outlet. The inlet temperature was fixed at 25 °C, and experiments were conducted at RH levels of 35% and 50%. The reaction bed had a square cross-section measuring 15 cm on each side, with a uniform porous composite layer height of 5 cm, ensuring a consistent volume across all tests. Temperature and humidity sensors continuously monitored both the inlet and outlet conditions at a frequency of 1 Hz throughout the 3-hour experimental period, providing comprehensive data for evaluating the sorption and heat release performance of the composites.

2.5. Desorption experiment

Desorption performance is critical for evaluating TCES composites, with dehydration temperature and desorption rate as key parameters. To comprehensively assess the desorption behavior of selected porous composites, two complementary experiments were conducted: isothermal desorption and thermogravimetric analysis–differential scanning calorimetry (TGA-DSC). Both experiments utilized samples that were pre-conditioned at 25 °C and 53% relative humidity for 48 h to achieve near-equilibrium moisture content.

The isothermal desorption experiment investigated desorption behavior under controlled temperature conditions. The pre-conditioned samples were placed in a temperature-controlled oven set at 90 °C and 150 °C. Weight measurements were recorded at 10-minute intervals

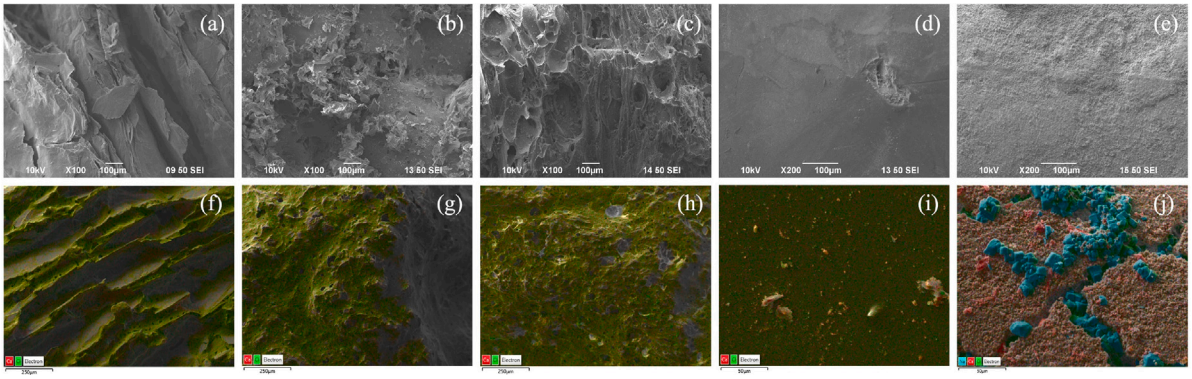


Fig. 6. SEM and SEM-EDX images of porous host materials before and after $CaCl_2$ impregnation: (a)–(e) represent untreated V, EP, Pm, SG, and Z, respectively; (f)–(j) show the corresponding impregnated composites with visible $CaCl_2$ distribution.

using a high-precision balance, providing detailed data on desorption kinetics. These data were further utilized to fit a first-order reaction kinetics model.

The second experiment employed TGA-DSC to simultaneously monitor weight loss and heat flow during the charging process. Preconditioned samples were analyzed using an SDT650 thermal analyzer, subjected to a controlled heating program from 20 °C to 200 °C at a consistent rate of 1 °C/min.

3. Results & discussion

3.1. Physical characterization

This section presents a detailed characterization of the porous host materials and their corresponding salt-infused composites, encompassing SEM and elemental distribution observations, density and salt content analysis and pore structure evaluations.

3.1.1. Morphological analysis

To examine the morphological changes and elemental distribution of porous host materials caused by $CaCl_2$ impregnation, SEM-EDX analyses were performed. The SEM images of untreated porous host materials and their corresponding impregnated composites are shown in Fig. 6.

The SEM-EDX analyses revealed substantial microstructural change and elemental distribution in the porous host materials before and after $CaCl_2$ impregnation. V (Fig. 6a) showed its typical layered structure with pronounced interlayer gaps prior to impregnation. After impregnation (Fig. 6f), $CaCl_2$ was uniformly distributed within the interlayer spaces and on the surface, filling these pores and reducing interlayer gaps. EP (Fig. 6b) exhibited a folded macroporous structure before treatment, and post-impregnation (Fig. 6g), $CaCl_2$ adhered to the pore walls, with some pores being partially or completely filled. Pm (Fig. 6c) initially showed interconnected pores, which were reduced in size after impregnation (Fig. 6h) due to $CaCl_2$ filling. SG (Fig. 6d) had fine pores that were difficult to observe at 200x magnification; and the EDX image after impregnation (Fig. 6i) revealed a uniform distribution of $CaCl_2$. Z (Fig. 6e) exhibited a spherical cluster structure with pores between the clusters. After impregnation (Fig. 6j), cracks were observed within the zeolite structure, and sodium chloride crystals were found forming inside these cracks.

3.1.2. Density and salt contents analysis

The physical properties of various porous host materials were examined to assess their suitability for TCES applications. A summary of these properties is provided in Table 2.

As shown in Table 2, macroporous materials such as EP and V exhibit high porosities (91.02% and 82.98%, respectively). In contrast, mesoporous SG and microporous Z have lower porosities (38.75% and 21.38%). The bulk density also varies significantly, with expanded perlite showing the lowest (0.0821 g/ml) and SG the highest (0.7858 g/ml).

Table 2
Summary of physical properties of five porous host materials.

Material	Shape	Average size (mm)	ρ_{bulk} (g/ml)	$\rho_{particle}$ (g/ml)	$\rho_{skeletal}$ (g/ml)	ϵ_{pore} (%)	ϵ_{void} (%)
V	Layered	$8.57 \times 9.86 \times 5.53$	0.1197	0.2605	1.5307	82.98	54.05
EP	Irregular	$4.7 \times 6 \times 3.84$	0.0821	0.1634	1.8192	91.02	49.76
Pm	Irregular	$2.96 \times 3.78 \times 4.48$	0.3952	0.7236	1.9086	62.09	45.38
SG	Spherical	∅4.09	0.7858	1.2961	2.1160	38.75	39.37
Z	Cylindrical	∅1.55, H5.10	0.6422	1.8839	2.3963	21.38	65.91

After vacuum impregnation, the porous materials were transformed into salt-impregnated composites, whose properties, including volumetric salt content (ϕ_v, g/ml) and predicted volumetric energy storage density (ESD_v, GJ/m^3), are summarized in Table 3. The volumetric expansion ratio (β) is defined as the ratio of the composite material's volume to the initial volume of the porous host materials before impregnation.

The predicted volumetric energy storage density (ESD_v) was calculated using the following equation:

$$ESD_v(\text{Predict}) = \frac{\phi_v \cdot \Delta H}{M_{CaCl_2}} \tag{4}$$

Here, ΔH is the enthalpy change associated with the $CaCl_2$ reaction (361.2 kJ/mol [44]), and M_{CaCl_2} denotes the molar mass of $CaCl_2$ (110.98 g/mol).

The bulk density of the composites increased in all samples as a result of salt loading. Particle density generally rose after impregnation. However, Z-$CaCl_2$ exhibited a decrease because its initial skeletal density of 2.20 g/ml was higher than the density of $CaCl_2$, which is approximately 2.15 g/ml. Volumetric expansion ratios (β) varied among the materials. V-$CaCl_2$ exhibited the highest volumetric expansion ratio at 1.375, as its folded, layered structure opened up during vacuum impregnation, allowing extensive salt uptake and resulting in a substantial decrease in porosity from 82.98% to 57.65%. SG-$CaCl_2$ showed minimal expansion due to fragmentation during impregnation, which reduced its void ratio from 39.37% to 34.74%. Other macroporous composites, such as EP-$CaCl_2$, experienced a notable porosity reduction from 91.02% to 57.84%, while Z-$CaCl_2$ showed a slight porosity increase from 21.38% to 21.94%, potentially due to micro-cracking caused by internal salt expansion.

V-$CaCl_2$ and EP-$CaCl_2$ exhibited notably high salt contents, both exceeding 65%. In contrast, Pm-$CaCl_2$, despite its large internal pores, showed a comparatively lower salt content of 24.19%, likely due to limited hydrophilicity. Z-$CaCl_2$, a typical microporous material, achieved a moderate salt content of 34.63%. However, SEM-EDX analysis revealed

Table 3
Properties of porous composite materials.

Symbol	Parameter (Unit)	V-$CaCl_2$	EP-$CaCl_2$	Pm-$CaCl_2$	SG-$CaCl_2$	Z-$CaCl_2$
ϕ_g	Gravimetric salt content (%)	66.13	69.21	24.19	15.96	34.63
ESD_g	Gravimetric ESD (kJ/kg)	2152.29	2252.54	787.30	519.44	1127.08
ρ_{bulk}	Bulk density (g/ml)	0.2655	0.2865	0.4493	0.9165	0.8573
$\phi_{v,b}$	Bulk volumetric salt content (g/ml)	0.1756	0.1983	0.1087	0.1463	0.2969
$ESD_{v,b}$	Bulk volumetric ESD (GJ/m^3)	0.5714	0.6454	0.3537	0.4761	0.9662
$\rho_{particle}$	Particle density (g/ml)	0.6881	0.6657	0.9473	1.4044	1.7179
$\phi_{v,p}$	Particle volumetric salt content (g/ml)	0.4550	0.4607	0.2292	0.2241	0.5949
$ESD_{v,p}$	Particle volumetric ESD (GJ/m^3)	1.4810	1.4995	0.7458	0.7295	1.9362
$\rho_{skeletal}$	Skeletal density (g/ml)	1.6247	1.5789	1.8535	2.1603	2.2007
ϵ_{pore}	Pore porosity (%)	57.65	57.84	48.89	34.99	21.94
ϵ_{void}	Void fraction (%)	61.42	56.96	52.57	34.74	50.10
β	Expansion ratio	1.375	1.05	1.18	1.00	1.15

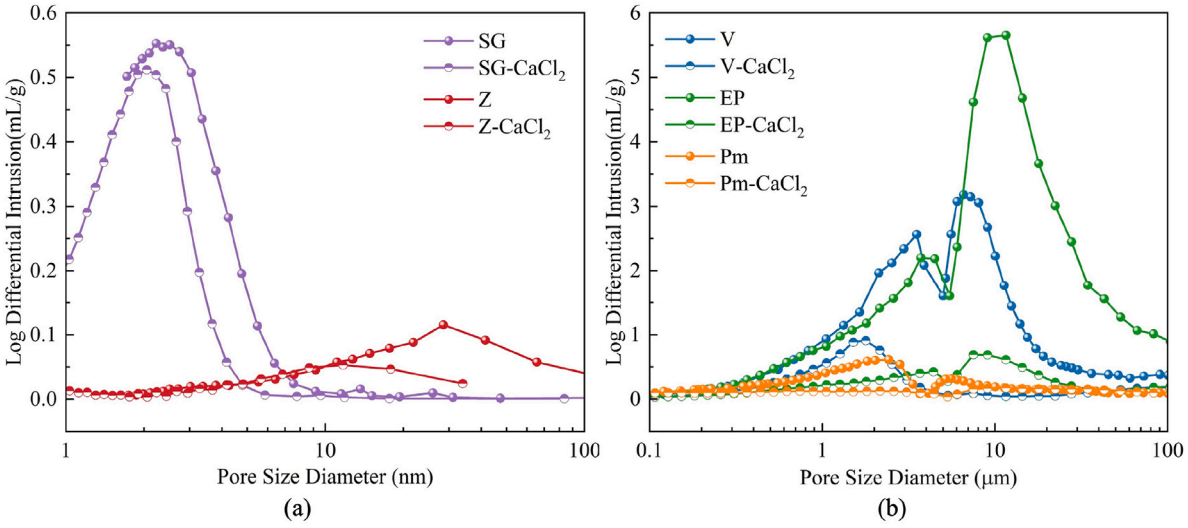


Fig. 7. Pore size distribution of porous materials and their $CaCl_2$-composites: (a) BET analysis for mesoporous (SG, Z); (b) MIP analysis for macroporous (V, EP, Pm).

that calcium ions from $CaCl_2$ can undergo ion exchange with sodium ions in the zeolite structure, forming sodium chloride crystals [45], which may lead to an overestimation of the actual $CaCl_2$ content.

The predicted volumetric energy storage density (ESD_v) values highlighted Z-$CaCl_2$ as having the highest theoretical potential, at 0.9662 GJ/m^3, although it could be influenced by ion exchange. EP-$CaCl_2$ and V-$CaCl_2$ followed with ESD_v values of 0.6454 GJ/m^3 and 0.5714 GJ/m^3, respectively. In comparison, SG-$CaCl_2$ and Pm-$CaCl_2$ displayed lower ESD_v values, measuring 0.4761 GJ/m^3 and 0.3537 GJ/m^3, respectively.

3.1.3. Pore structure analysis

Pore size distribution for mesoporous materials (SG) and microporous materials (Z) was determined using the BET method, while MIP analysis was utilized for macroporous materials (V, EP, and Pm). Fig. 7 and Table 4 offer detailed insights into the pore parameters of untreated porous host materials and their resulting composites.

Based on Fig. 7 and Table 4, macroporous materials V, EP, and Pm exhibit higher pore volumes and lower specific surface areas, while mesoporous SG and microporous Z demonstrate smaller pore volumes and higher specific surface areas. The average pore diameter of SG, below 10 nm, confirms its mesoporous nature. Z, with an average pore diameter of 14.13 nm measured by BET analysis, aligns with values reported in other studies [21,46], although its internal repeating units feature pore diameters of 0.8–0.9 nm [47]. In contrast, Pm shows an average pore size of approximately 200 nm, while V and EP exhibit pore sizes in the micron range.

Table 4
Pore volume, average pore diameter, and specific surface area of various porous host materials and their composites.

Samples	V_{pore} (ml/g)	D_{avg} (nm)	SSA (m^2/g)
V	3.1849	2047.25	6.22
V-$CaCl_2$	0.8377	484.75	6.91
P	5.5702	3211.49	6.94
EP-$CaCl_2$	0.8688	706.76	4.92
Pm	0.8581	195.46	17.56
Pm-$CaCl_2$	0.5161	174.94	11.80
SG	0.2334	2.77	437.66
SG-$CaCl_2$	0.2322	1.64	284.13
Z	0.1107	14.13	32.47
Z-$CaCl_2$	0.0566	5.20	155.41

After $CaCl_2$ impregnation, all porous composites displayed notable reductions in pore volume and average pore diameter, confirming effective salt loading. V-$CaCl_2$ and EP-$CaCl_2$ showed the most significant decreases in pore volume, with V-$CaCl_2$ reducing from 3.1849 ml/g to 0.8377 ml/g and EP-$CaCl_2$ from 5.5702 ml/g to 0.8688 ml/g, reflecting their capacity to incorporate $CaCl_2$ into their expansive pore structures. SG-$CaCl_2$ had an initial pore volume of 0.2334ml/g, which remained nearly unchanged after impregnation at 0.2322ml/g, but its average pore diameter decreased from 2.77 nm to 1.64 nm. Z-$CaCl_2$ exhibited similar trends, with its pore volume reducing from 0.1107 ml/g to 0.0566 ml/g and its average pore diameter shifting from 14.13 nm to 5.20 nm. Pm-$CaCl_2$, starting with a moderate pore volume of 0.8581 ml/g and an average pore diameter of 195.46 nm, experienced reductions to 0.5161 ml/g and 174.94 nm, respectively.

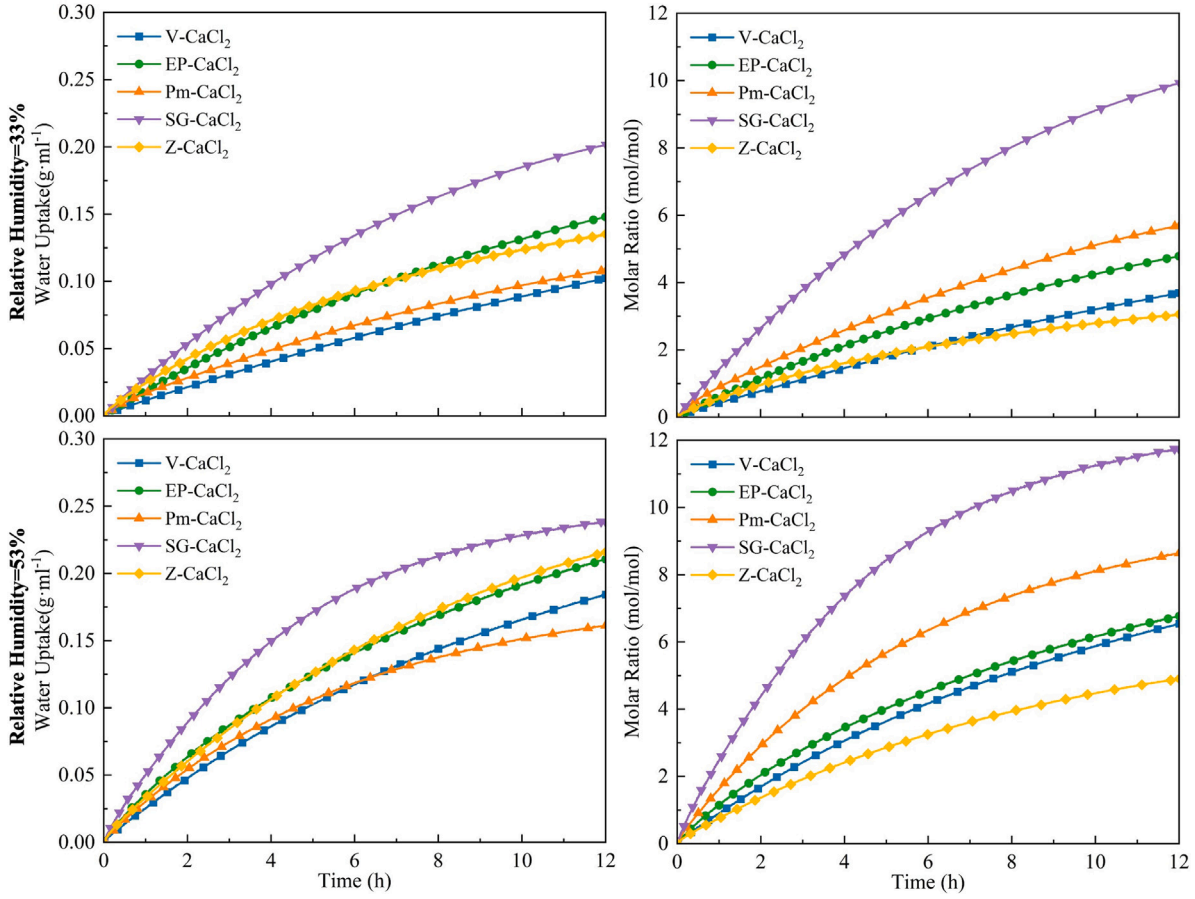


Fig. 8. Sorption performance of five porous composites at relative humidity levels of 33% and 53%.

Table 5
Summary of fitting parameters for water uptake of composite at relative humidity levels of 33% and 53%.

Sample	RH = 33%					RH = 53%				
	k (1/h)	t_{90} (h)	w_e (g/ml)	χ_e (mol/mol)	R^2	k (1/h)	t_{90} (h)	w_e (g/ml)	χ_e (mol/mol)	R^2
V-$CaCl_2$	0.0441	52.26	0.2479	8.943	1.0000	0.0844	27.27	0.2887	10.240	0.9999
EP-$CaCl_2$	0.0744	30.95	0.2501	8.079	1.0000	0.0961	23.96	0.3059	9.838	0.9993
Pm-$CaCl_2$	0.0858	26.84	0.1657	8.723	0.9996	0.1611	14.29	0.1888	10.120	0.9999
SG-$CaCl_2$	0.1215	18.95	0.2611	12.860	0.9995	0.2160	10.66	0.2580	12.700	0.9999
Z-$CaCl_2$	0.1139	20.22	0.1800	4.066	0.9994	0.1108	20.78	0.2925	6.642	1.0000

3.2. Static sorption performance analysis

The sorption performance of porous composite, including both reaction rate and equilibrium moisture sorption capacity, is strongly influenced by temperature and humidity, particularly relative humidity [48]. To evaluate their actual sorption performance, five types of composites were tested under relative humidity levels of 33% and 53%. The results are presented in Fig. 8.

Based on the static water uptake curves, a first-order kinetic model was used to fit the data, and the time required to reach 90% of the equilibrium water uptake (t_{90}) was calculated for each sample. The fitting results are summarized in Table 5. For a first-order reaction, t_{90} can be derived using the formula:

$$t_{90} = \frac{-\ln(1-0.9)}{k} = \frac{2.3026}{k} \tag{5}$$

From the water uptake curves and fitting parameters, it is evident that different composite exhibit variations in reaction rates and equilibrium water uptake under varying humidity conditions. In general, both reaction rate and equilibrium water uptake increase with higher relative humidity, consistent with theoretical predictions. Among the five tested composites, SG-$CaCl_2$ demonstrates the fastest reaction rate, with t_{90} values of 18.95 h at RH = 33% and 10.66 h at RH = 53%, significantly outperforming the other composites. This rapid reaction is attributed to its high specific surface area, which facilitates efficient water vapor sorption and accelerates reaction kinetics. In contrast, Z-$CaCl_2$ exhibits a moderate reaction rate that remains unchanged across humidity levels. While equilibrium water uptake increases with higher humidity, the molar ratio remains low, rising from $\chi_e = 4.066$ mol/mol at RH = 33% to $\chi_e = 6.642$ mol/mol at RH = 53%. This behavior suggests ion exchange reactions within Z-$CaCl_2$ may reduce its sorption capacity.

For macroporous composites, V-$CaCl_2$ and EP-$CaCl_2$ exhibit higher equilibrium water uptake under high humidity, reflecting their high salt content and enhanced capacity for sustained heat release. However, their reaction rates are slower, likely due to pore blockage and relatively small specific surface areas, which limit water vapor diffusion. In contrast, Pm-$CaCl_2$, while demonstrating the fastest reaction rate among macroporous composites, achieves lower equilibrium water uptake, attributed to its lower salt content and higher specific surface area.

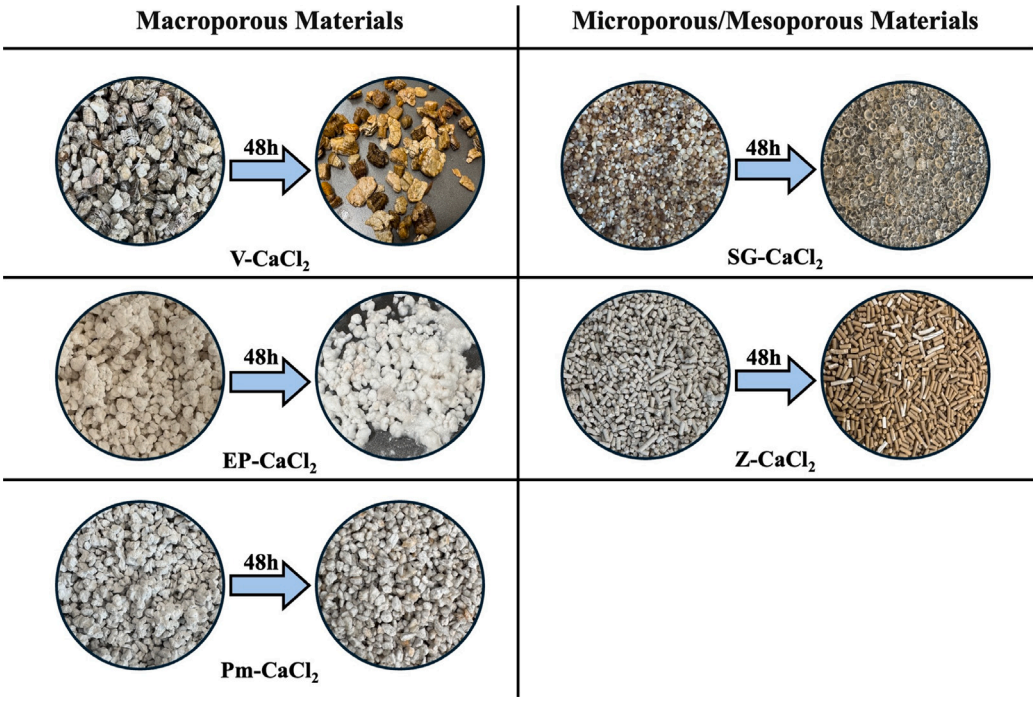


Fig. 9. Morphology of porous composites after 48-hour exposure to RH = 53% under controlled temperature conditions.

To evaluate structural stability, samples were exposed to RH = 53% in a temperature-controlled chamber for 48 h. The resulting morphologies, shown in Fig. 9, reveal differences in the composites' ability to accommodate excessive hydration.

As shown in Fig. 9, V-$CaCl_2$ exhibits a moist surface after excessive hydration, with retained solution in its layered pores causing a softened texture. EP-$CaCl_2$ develops a porridge-like consistency, indicating significant structural damage. In contrast, Pm-$CaCl_2$ retains structural integrity and hardness despite minor solution leakage. SG-$CaCl_2$, while becoming slightly transparent upon water absorption, shows minimal solution leakage and maintains its hardness. Z-$CaCl_2$, with its relatively low hygroscopic capacity, shows no solution leakage but experiences a slight reduction in hardness. Overall, V-$CaCl_2$ and SG-$CaCl_2$ demonstrate better accommodation of excessive hydration, maintaining structural integrity and effectively containing solution within their capillary networks.

3.3. Dynamic performance analysis

The thermal energy release and moisture sorption characteristics of five porous composite were evaluated in a small-scale reactor, as depicted in Fig. 10.

Fig. 10 shows that SG-$CaCl_2$ achieved the highest peak temperatures under both RH = 35% and RH = 50% conditions, reaching 40.28 °C and 46.27 °C, respectively, along with the lowest outlet relative humidity. This highlights its superior sorption and heat release performance. However, its high thermal capacity results in a slower thermal response, taking about 30 min to reach peak temperature compared to 20 min for the other composites.

Higher inlet humidity enhanced the heat release performance of all composites, leading to increased peak temperatures. Among them, EP-$CaCl_2$ demonstrated the second-best heat release performance under both humidity conditions. Meanwhile, Z-$CaCl_2$ showed a notable increase in peak temperature with rising relative humidity, from 36.25 °C to 41.98 °C. Its output characteristics were similar to those of EP-$CaCl_2$, though with slightly lower output temperatures. In contrast, V-$CaCl_2$ and Pm-$CaCl_2$ exhibited lower outlet temperatures under both humidity conditions, which corresponded to their higher outlet relative humidity values. The residual temperature rise after three hours followed the order: SG-$CaCl_2$ >EP-$CaCl_2$ >Z-$CaCl_2$ >Pm-$CaCl_2$ >V-$CaCl_2$.

To further analyze the thermal performance of these composites under varying humidity levels, violin plots were employed to visualize the temporal statistical distribution of temperature rise (ΔT) and outlet relative humidity, as shown in Fig. 11.

These plots provide a comprehensive depiction of both central tendencies (mean values, T_{avg} or RH_{avg}) and the probability density distribution. The contours of the violin plots represent the frequency of specific values over time, with higher sections indicating higher frequencies. Solid lines denote mean values, while dashed lines represent the first quartile (Q_1) and third quartile (Q_3).

As shown in Fig. 11, SG-$CaCl_2$ demonstrated the highest average temperature rise and the lowest average outlet relative humidity under both humidity conditions. For approximately half of the operating period, its temperature rise ranged from 11.91–14.45 °C at RH = 35% and 16.01–20.13 °C at RH = 50%. EP-$CaCl_2$ recorded the second-highest average temperature rise, with values of 7.98 °C and 12.51 °C under RH = 35% and RH = 50%, respectively. It also exhibited smoother temperature decay, with approximately half the time spent above the average temperature and the other half below it. In contrast, V-$CaCl_2$, Pm-$CaCl_2$, and Z-$CaCl_2$ showed faster temperature decay after reaching their peaks, spending most of the operating period in the low-temperature range.

The heat release, water uptake, and pressure drop of five porous composites were evaluated over a 3-hour period under varying conditions to compare their performance in dynamic sorption processes. The results are summarized in Fig. 12.

These metrics were calculated by integrating the instantaneous relative humidity difference and temperature rise between the inlet and outlet over time, which respectively represent the cumulative water uptake and total heat release. The water uptake and heat release were normalized by the reaction bed volume. Additionally, the pressure drop across the packed bed was measured to account for differences in the

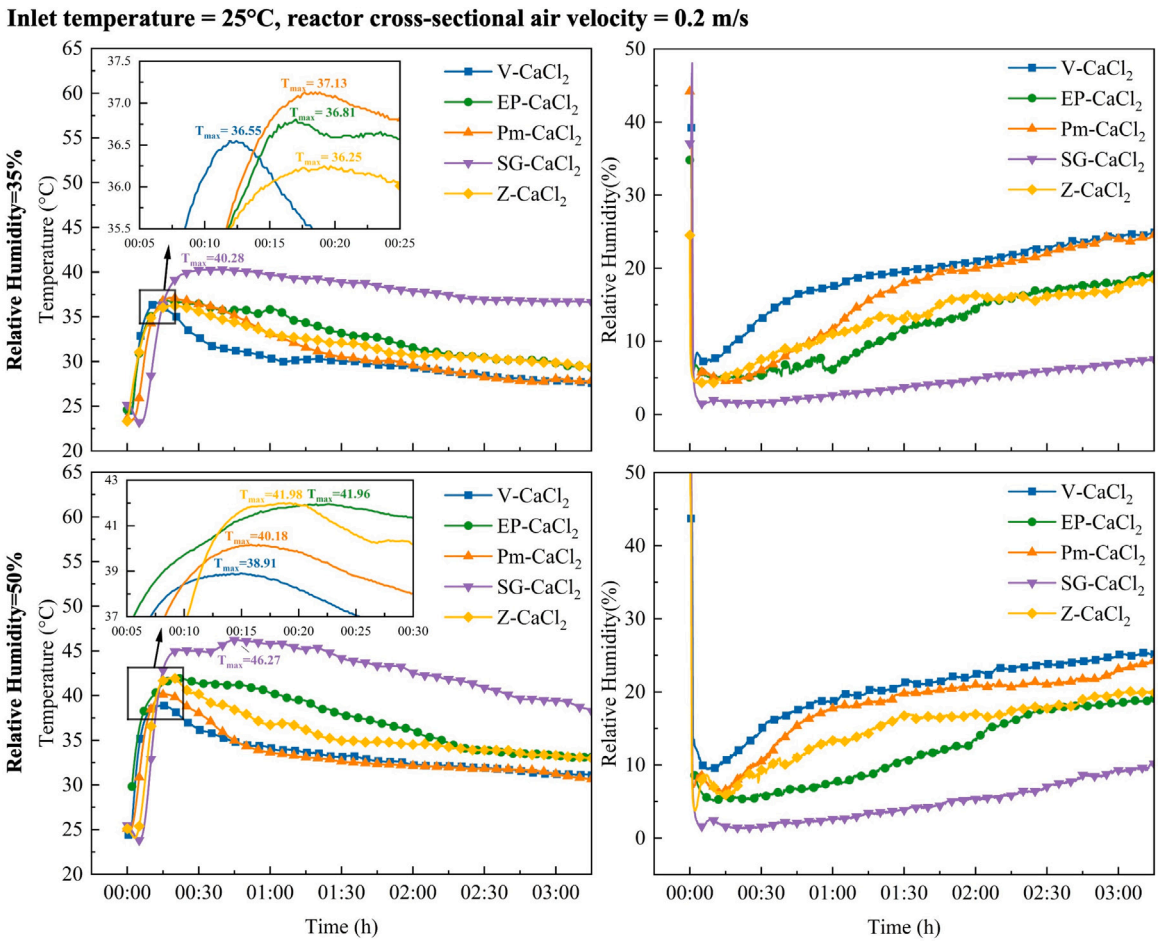


Fig. 10. Outlet temperature and relative humidity profiles over time for different porous composite.

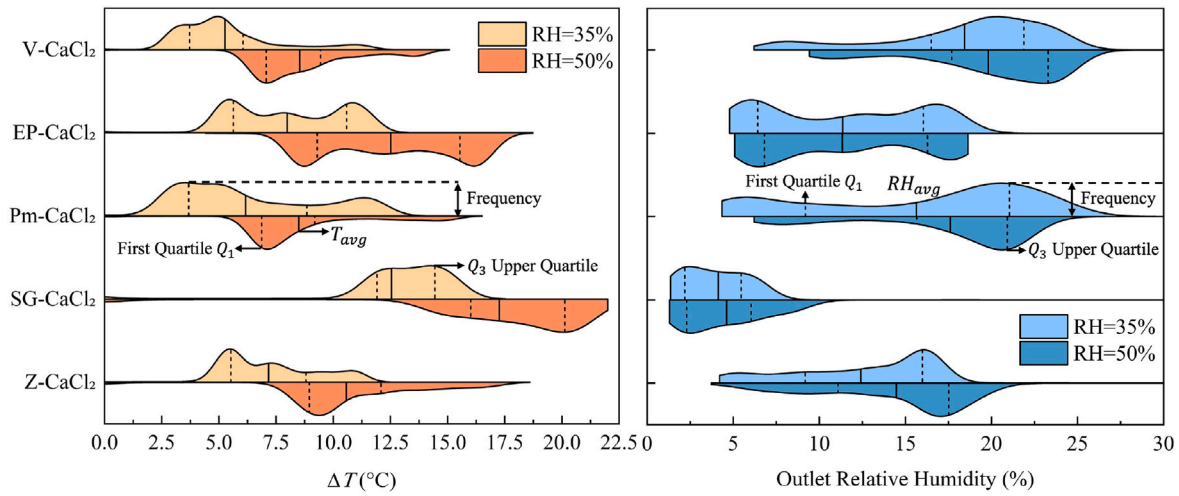


Fig. 11. Violin plots of temperature rise (ΔT) and outlet relative humidity for five porous composites under RH = 35% and RH = 50%.

packing characteristics of these porous composites, as the pressure drop is influenced by the void volume and particle arrangement within the reaction bed.

From Fig. 12, it can be observed that under both relative humidity conditions, there is an approximately linear relationship between the water uptake and the heat release of the reactor bed. On average, each gram of water absorbed during the reaction generates about 2.45 kJ/g of heat release. This value is slightly lower than the theoretical heat release of 60.2 kJ/mol of water absorbed (approximately 3.34 kJ/g [44]). The observed discrepancy can be attributed to factors such as potential measurement inaccuracies and heat losses from the reactor, which reduce the measured heat release compared to the theoretical expectation.

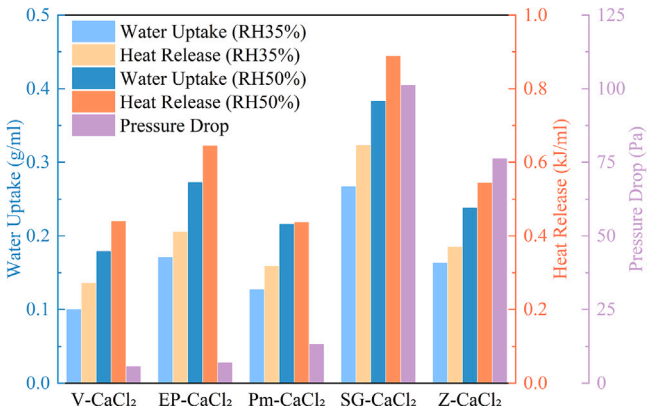


Fig. 12. Total heat release, water uptake, and pressure drop for five porous composites over a 3-hour period under varying conditions.

Table 6
Desorption reaction constants and equilibrium times for different composite at 90 °C and 150 °C.

Sample	T = 90 °C			T = 150 °C		
	k (1/h)	t_{90} (h)	R^2	k (1/h)	t_{90} (h)	R^2
V-$CaCl_2$	0.983	2.342	0.9982	1.607	1.433	0.9968
EP-$CaCl_2$	0.761	3.026	0.9999	2.062	1.117	0.9994
Pm-$CaCl_2$	1.462	1.575	0.9994	2.987	0.771	0.9933
SG-$CaCl_2$	0.916	2.513	0.9997	2.582	0.892	0.9995
Z-$CaCl_2$	0.811	2.838	0.9980	3.346	0.688	0.9938

Among the tested composites, SG-$CaCl_2$ showed the highest water uptake and heat release under both humidity conditions. However, it also exhibited the highest pressure drop across the packed bed, reaching 101.06 Pa, due to its compact packing structure and relatively small void volume. Z-$CaCl_2$, while demonstrating moderate water uptake and heat release, exhibited a relatively high pressure drop of 76.09 Pa. EP-$CaCl_2$, ranking second in both water uptake and heat release, achieved a much lower pressure drop of 6.88 Pa, indicating lower airflow resistance. Macroporous composites such as V-$CaCl_2$ and Pm-$CaCl_2$ exhibited lower water uptake and heat release but maintained the lowest pressure drops, at 5.61 Pa and 13.17 Pa, respectively. The cumulative water uptake trend is consistent with findings from static moisture sorption experiments.

3.4. Desorption performance analysis

To evaluate the desorption properties of the five porous composites, their isothermal desorption weight loss curves were analyzed using a constant temperature oven. Fig. 13 presents the desorption weight loss curves of the composites alongside their corresponding hydration level change curves.

It can be observed that at a drying temperature of 150 °C, complete desorption is achieved for all the composite, whereas at 90 °C, only partial desorption to a hydration level of 3–5 is observed in all but the Z-$CaCl_2$ composite. The near-complete dehydration of Z-$CaCl_2$ at 90 °C is hypothesized to be influenced by ion-exchange effects, which may have altered the properties. Among the other composites, EP-$CaCl_2$ shows the highest dehydration at 90 °C, with a 75% reduction in mass relative to its initial weight. This is followed by Pm-$CaCl_2$ and SG-$CaCl_2$, both showing a 72.5% decrease, while the lowest reduction is observed in V-$CaCl_2$, at only 66.2%. To compare the desorption rates quantitatively, first-order reaction kinetics models were applied to fit the desorption data at both temperatures. The calculated desorption reaction constants are summarized in Table 6.

The results in Table 6 show that the first-order reaction kinetic model provides an excellent fit for the desorption curves. At 90 °C, Pm-$CaCl_2$ exhibited the highest desorption rate constant, reaching near-equilibrium in just 1.58 h, likely due to its efficient internal heat transfer properties. V-$CaCl_2$ and SG-$CaCl_2$ followed with moderate desorption rates and equilibrium times of 2.34 and 2.51 h, respectively. Although Z-$CaCl_2$ achieved the highest desorption weight loss (Δw = 0.28 g/ml), its equilibrium time of 2.84 h indicates only moderate kinetic performance. In contrast, EP-$CaCl_2$, despite achieving a high dehydration fraction (Δw = 0.26 g/ml), exhibited the slowest desorption rate and the longest equilibrium time (t_{90} = 3.03 h) among the samples.

At 150 °C, the desorption rate constants increased significantly for all samples. Z-$CaCl_2$ showed the most substantial improvement, with its equilibrium time decreasing from 2.84 h at 90 °C to just 0.69 h, making it the fastest to reach equilibrium. Pm-$CaCl_2$ maintained strong performance, ranking second with an equilibrium time of 0.77 h. SG-$CaCl_2$ also demonstrated a significant improvement, achieving equilibrium in 0.89 h. Although EP-$CaCl_2$ exhibited a slightly faster desorption rate than V-$CaCl_2$ at the higher temperature, it remained less competitive in kinetic performance compared to Pm-$CaCl_2$, SG-$CaCl_2$, and Z-$CaCl_2$.

To study the desorption characteristics of the composites, thermogravimetric analysis and differential scanning calorimetry (TGA-DSC) were conducted. TGA tracks weight changes as a function of temperature, while DSC monitors heat flow, offering a combined analysis of thermal events and desorption behavior. The weight loss data were further processed to generate derivative thermogravimetric (DTG) curves, which pinpoint the temperature ranges associated with distinct desorption stages. The results are presented in Fig. 14.

V-$CaCl_2$ exhibits a minor weight loss peak in the 50–70 °C range, followed by a major weight loss between 90–130 °C, indicating the presence of two distinct dehydration stages. EP-$CaCl_2$ displays two prominent weight loss peaks at 50–70 °C and 85–125 °C, with the desorption process nearly complete by 125 °C. In contrast, the weight loss for V-$CaCl_2$ extends up to 150 °C, likely due to the lower permeability of its layered pore structure. Pm-$CaCl_2$ exhibits a single pronounced weight loss peak between 70–125 °C. Mesoporous composites, such as SG-$CaCl_2$ and Z-$CaCl_2$, show smoother weight loss curves compared to macroporous composites, which may be attributed to their higher internal binding energy. Z-$CaCl_2$ displays an initial weight loss peak around 50 °C and a secondary, smaller peak at 155 °C. Similarly, SG-$CaCl_2$ exhibits an endothermic peak in the 50–70 °C range.

To further investigate the thermal characteristics during desorption, DSC analysis was conducted simultaneously with TGA, and the results are presented in Fig. 15.

The DSC curves reveal that all composite exhibit two distinct endothermic peaks. The first peak is concentrated around 58 °C, with a pronounced depth indicating significant heat sorption within this temperature range. The position of the second endothermic peak varies among the composite. EP-$CaCl_2$ exhibits the earliest second peak, appearing at around 110 °C. Pm-$CaCl_2$, SG-$CaCl_2$, and Z-$CaCl_2$ show less distinct second peaks, occurring around 115 °C. The latest second peak is observed for V-$CaCl_2$, appearing near 125 °C.

Integrating insights from the DTG curves, the dehydration process of $CaCl_2$ can be broadly divided into two stages. The first weight loss peak occurs at 58 °C, where the weight loss rate is relatively low but the heat sorption is significant. Macroporous composites exhibit more distinct peak changes, indicating a concentrated thermal effect during desorption. In contrast, mesoporous composites, such as SG-$CaCl_2$, display smoother curves across the entire temperature range, suggesting a more gradual and distributed heat sorption process. This behavior may be attributed to the higher internal molecular bonding energy within the mesoporous structure.

3.5. Discussion

This study provides a detailed evaluation of the sorption and desorption performance of five porous composites prepared via vacuum impregnation. Key findings, summarized in Table 7, highlight the unique advantages and challenges associated with each composite.

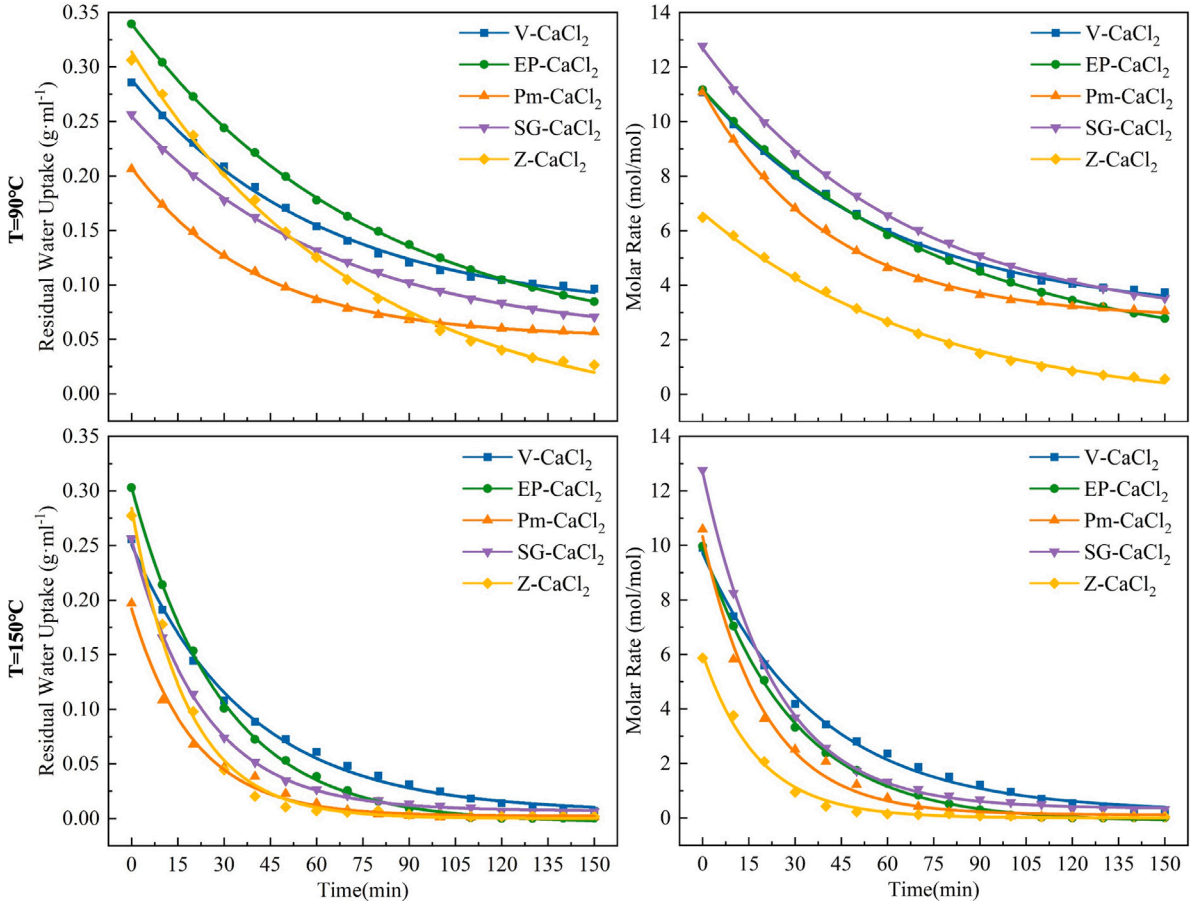


Fig. 13. Isothermal desorption weight loss curves and corresponding hydration level change curves of five porous composites at different temperatures (150 °C, 90 °C).

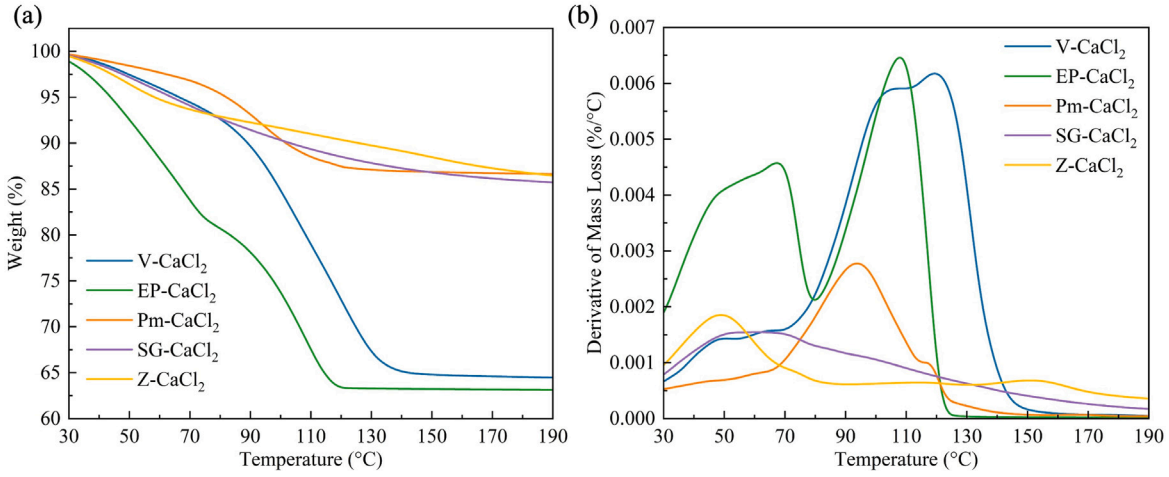


Fig. 14. Thermogravimetric analysis (TGA) of the porous composites. (a) Weight loss curves and (b) derivative thermogravimetric (DTG) curves.

From a physical parameter perspective, V-$CaCl_2$ and EP-$CaCl_2$, with their high porosity, achieved gravimetric salt contents exceeding 65%, resulting in relatively high volumetric energy storage densities (0.55–0.65 GJ/m^3). Despite the relatively low gravimetric salt content of Z-$CaCl_2$, its high bulk density contributed to the highest volumetric salt content (0.2378 g/ml). However, SEM-EDX analysis revealed the formation of sodium chloride crystals from ion exchange, which could lead to an overestimation of its true volumetric energy storage density. Mesoporous composites such as SG-$CaCl_2$, with superior bulk-specific surface area, exhibited better sorption performance compared to macroporous composites.

During discharging experiments, SG-$CaCl_2$ demonstrated the fastest sorption rate and the highest equilibrium molar ratio, driven by both physical and chemical sorption mechanisms. Pm-$CaCl_2$, with a moderate salt content, ranked second in sorption rate, outperforming Z-$CaCl_2$. This suggests that ion exchange significantly altered the sorption

Table 7
Physical parameters, discharging performance, and charging performance of various porous composites.

Sample	V-$CaCl_2$	EP-$CaCl_2$	Pm-$CaCl_2$	SG-$CaCl_2$	Z-$CaCl_2$
Porosity (%)	57.65	57.84	48.89	34.99	21.94
Bulk SSA_v (m^2/cm^3)	1.83	1.41	5.30	260.41	133.23
Gravimetric salt content (%)	66.13	69.21	24.19	15.96	34.63
Volumetric salt content (g/ml)	0.1756	0.1983	0.1087	0.1463	0.2969
Particle ESD_v (GJ/m^3)	1.4810	1.4995	0.7458	0.7295	1.9362
Bulk ESD_v (GJ/m^3)	0.5714	0.6454	0.3537	0.4761	0.9662
Discharging reaction rate	Slowest	Slow	Fast	Fastest	Medium
Equilibrium sorption weight (g/ml)	0.2887	0.3059	0.1888	0.2580	0.2925
Equilibrium molar ratio (mol/mol)	10.24	9.84	10.12	12.70	6.64
Capacity to accommodate overhydration	Good	Poor	Poor	Good	Average
Average output temperature	Low	High	Low	Highest	Medium
Temperature decay rate	Fast	Slow	Fast	Slow	Medium
Reaction bed pressure drop	Low	Low	Medium	Very High	High
Low-temperature charging reaction rate	Fast	Slow	Fastest	Fast	Medium
High-temperature charging reaction rate	Slow	Medium	Fast	Medium	Fastest

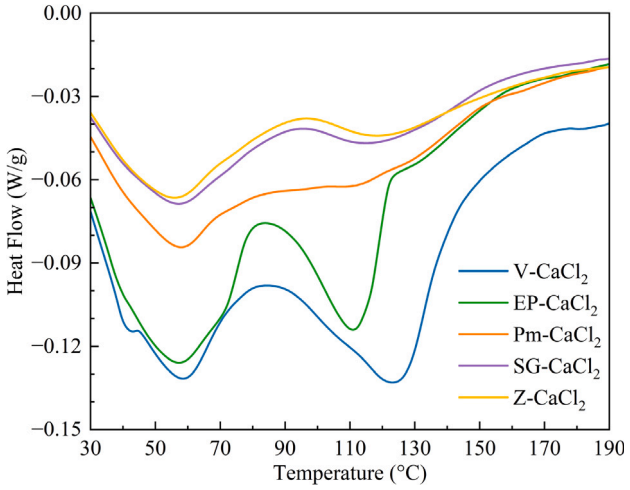


Fig. 15. DSC curves illustrating heat flow during the desorption process for different composites.

characteristics of Z-$CaCl_2$. Among macroporous composites, EP-$CaCl_2$ achieved the highest volumetric equilibrium sorption weight, while V-$CaCl_2$, despite its relatively large, underperformed due to inefficient mass transfer within its layered structure. Under overhydration conditions, V-$CaCl_2$ and SG-$CaCl_2$ demonstrated excellent solution containment capacity, while EP-$CaCl_2$ suffered irreversible structural damage, underscoring the importance of controlling hydration levels in practical applications.

In reactor-level experiments, SG-$CaCl_2$ achieved the highest output temperature and the slowest temperature decay, albeit with a significant reactor pressure drop. EP-$CaCl_2$ delivered favorable performance with moderate sorption rates. It achieved the second-highest average output temperature, along with slow temperature decay and minimal pressure drop. Z-$CaCl_2$ exhibited output characteristics similar to EP-$CaCl_2$, though it experienced faster temperature decay. By contrast, V-$CaCl_2$ and Pm-$CaCl_2$ displayed rapid temperature decay after reaching their peaks, with low output temperatures dominating the discharging period.

In the charging experiments, Z-$CaCl_2$ achieved near-complete desorption at 90 °C due to ion exchange, a behavior that warrants further investigation. At 150 °C, Z-$CaCl_2$ exhibited the fastest desorption rate, followed by Pm-$CaCl_2$, while V-$CaCl_2$ showed the slowest rate due to poor mass transfer in its layered pore structure. SG-$CaCl_2$ and EP-$CaCl_2$ displayed moderate desorption performance.

Overall, SG-$CaCl_2$ and EP-$CaCl_2$ emerged as promising candidates for large-scale thermochemical energy storage systems. SG-$CaCl_2$ offers rapid heat release, high structural stability, and elevated output temperatures, although its high-pressure drop poses design challenges. EP-$CaCl_2$, with high volumetric energy storage density and stable heat output, provides a practical solution with minimal pressure drop, but requires careful hydration control. The unique behavior of Z-$CaCl_2$ under low-temperature charging conditions suggests potential for enhancing thermodynamic efficiency, warranting further study. V-$CaCl_2$ and Pm-$CaCl_2$ may be better suited for specialized applications: V-$CaCl_2$ excels in low-temperature, long-duration heat release, while Pm-$CaCl_2$ is less suitable for packed bed systems due to its lower energy density and inability to retain deliquescent solution.

4. Conclusions

This study evaluated the TCES performance of five porous composites with varying pore structures, prepared via vacuum impregnation. By investigating their sorption and desorption behaviors at both the particle and reactor levels, several key conclusions were drawn:

(1) Pore structure significantly affects salt content and energy storage density. Macroporous composites (V-$CaCl_2$ and EP-$CaCl_2$) achieved high gravimetric salt contents (>65%), resulting in moderate volumetric energy storage densities (ESD_v = 0.57–0.64 GJ/m^3). Despite its lower gravimetric salt content, Z-$CaCl_2$ exhibited the highest volumetric salt content (0.30 g/ml) and an estimated $ESD_v \approx 1\,GJ/m^3$, although ion exchange reactions may have led to an overestimation of its performance.

(2) Mesoporous SG-$CaCl_2$ achieved the fastest reaction rates and the highest equilibrium hydration level. With $\chi_e = 12.7$, this composite delivered sustained high-temperature output but suffered from high-pressure drop, limiting its scalability in packed bed systems. Conversely, macroporous EP-$CaCl_2$ offered an optimized trade-off, achieving the highest volumetric sorption weight ($w_e = 0.31$ g/ml) with minor pressure drop (8.07 Pa), making it a strong candidate for applications requiring low operational resistance.

(3) Desorption performance is highly temperature-dependent. At 90 °C, Z-$CaCl_2$ uniquely achieved near-complete desorption, likely due to ion exchange reactions altering its structure. At 150 °C, Pm-$CaCl_2$ exhibited the fastest desorption rate (t_{90} = 45 mins), followed by SG-$CaCl_2$ and Z-$CaCl_2$, demonstrating their suitability for rapid regeneration. Derivative thermogravimetric curves revealed that macroporous composites displayed distinct two-stage weight loss peaks and completed desorption by 150 °C, while mesoporous composites desorbed more gradually due to stronger binding energy.

This work bridges material-level synthesis with reactor-level evaluation, identifying EP-$CaCl_2$ as the most promising candidate for large-scale TCES systems due to its optimal balance of high water uptake (0.3059 g/ml), moderate volumetric energy density (0.6454 GJ/m^3), and low pressure drop (8.07 Pa). While SG-$CaCl_2$ achieves the fastest reaction rates and highest output temperatures, its scalability is limited by high-pressure drop. These findings emphasize the importance of integrating dynamic performance metrics into material optimization to advance scalable and reliable TCES systems. Future efforts should prioritize enhancing material durability under long-term cycling, investigating the interplay between salt loading and reaction kinetics, and further refining reactor-level designs to support the widespread deployment of efficient and reliable energy storage solutions.

Abbreviations

Abbreviation	Full Term
BET	Brunauer–Emmett–Teller (analysis method)
CSPM	Composite 'Salt Inside Porous Matrix'
DRH	Deliquescence Relative Humidity
DSC	Differential Scanning Calorimetry
DTG	Derivative Thermogravimetric
ESD	Energy Storage Density
ICP-OES	Inductively Coupled Plasma Optical Emission Spectrometry
MIP	Mercury Intrusion Porosimetry
RH	Relative Humidity
SEM	Scanning Electron Microscopy
SG	Silica Gel
SSA	Specific Surface Area
TGA	Thermogravimetric Analysis
TCES	Thermochemical Energy Storage
V	Vermiculite
EP	Expanded Perlite
Pm	Pumice
Z	Zeolite 13x

Nomenclature

Symbol	Description
D_{avg}	Average pore diameter (nm)
ESD_g	Gravimetric energy storage density (kJ/kg)
ESD_v	Volumetric energy storage density (GJ/m^3)
k	Reaction rate constant (1/h)
$m(t)$	Mass of the sample at time t (g)
$m(t_0)$	Initial mass of the sample (g)
M_{CaCl_2}	Molar mass of $CaCl_2$ (110.98 g/mol)
M_{H_2O}	Molar mass of water (18.01 g/mol)
n_{CaCl_2}	Moles of $CaCl_2$ (mol)
n_{H_2O}	Moles of water (mol)
RH_{avg}	Average relative humidity (%)
SSA	Specific surface area (m^2/g)
SSA_v	Volumetric specific surface area (m^2/cm^3)
T_{avg}	Average temperature (°C)
t	Time (h)
t_{90}	Time to reach 90% equilibrium (h)
V_{pore}	Pore volume per unit mass (cm^3/g)
$w(t)$	Water uptake at time t per unit volume (g/ml)
w_e	Equilibrium water uptake per unit volume (g/ml)

Greek symbols

Symbol	Description
β	Volumetric expansion ratio
ε_{pore}	Porosity (%)
ε_{void}	Void fraction (%)
ϕ	Salt content (%)
ϕ_g	Gravimetric salt content (%)
ϕ_v	Volumetric salt content (g/ml)
χ_e	Equilibrium hydration number (moles of water per mole of salt)
ΔH	Reaction enthalpy change (kJ/mol)
ΔT	Temperature rise (°C)
ρ_{bulk}	Bulk density (g/ml)
$\rho_{particle}$	Particle density including internal pores (g/ml)
$\rho_{skeletal}$	Skeletal density of the solid framework (g/ml)

Subscripts

Subscript	Description
avg	Average
b, bulk	Bulk properties
g	Gravimetric properties
p, particle	Particle properties
pore	Related to the pores within particles
skeletal	Skeletal properties of the solid framework
v	Volumetric properties
void	Void fraction between particles

CRediT authorship contribution statement

Jianbin Chen: Visualization, Methodology, Investigation, Formal analysis, Data curation. **Yong Zhang:** Writing – review & editing, Supervision, Methodology, Conceptualization. **Ziwei Chen:** Writing – review & editing, Supervision, Formal analysis. **Guohui Gan:** Writing – review & editing. **Yuehong Su:** Writing – review & editing, Supervision, Project administration, Funding acquisition, Conceptualization.

Declaration of competing interest

The authors declare that they have no known competing financial interests or personal relationships that could have appeared to influence the work reported in this paper.

Acknowledgments

This research was funded by the UK Research and Innovation (Horizon Europe Guarantee grant number: 10059624) and the European Union's Horizon Europe research and innovation program within the ECHO project, under grant agreement No. 101096368. The first author would also like to thank China Scholarship Council for providing his Ph.D. studentship.

References

[1] IEA, World Energy Outlook 2024, Tech. rep., IEA, Paris, France, 2024.
[2] IEA, Energy end-uses and efficiency indicators data explorer – data tools, 2021, https://www.iea.org/data-and-statistics/data-tools/energy-end-uses-and-efficiency-indicators-data-explorer. (Accessed November 25, 2024),
[3] L.C. Sögütoglu, P.A.J. Donkers, H.R. Fischer, H.P. Huinink, O.C.G. Adan, In-depth investigation of thermochemical performance in a heat battery: Cyclic analysis of K2CO3, MgCl2 and Na2S, Appl. Energy 215 (2018) 159–173, http://dx.doi.org/10.1016/j.apenergy.2018.01.083.

[4] F. Desai, J. Sunku Prasad, P. Muthukumar, M.M. Rahman, Thermochemical energy storage system for cooling and process heating applications: A review, Energy Convers. Manage. 229 (2021) 113617, http://dx.doi.org/10.1016/j.enconman.2020.113617.
[5] S. Roger-Lund, J. Darkwa, M. Worall, J. Calautit, R. Boukhanouf, A review of thermochemical energy storage systems for district heating in the UK, Energies 17 (14) (2024) 3389, http://dx.doi.org/10.3390/en17143389.
[6] Y. Zhang, M. Hu, Z. Chen, Y. Su, S. Riffat, Modelling analysis of a solar-driven thermochemical energy storage unit combined with heat recovery, Renew. Energy 206 (2023) 722–737, http://dx.doi.org/10.1016/j.renene.2023.02.076.
[7] T. Yan, T. Xie, W.G. Pan, L.W. Wang, Experimental study on ammonia-based thermochemical resorption thermal energy storage system, Renew. Energy 229 (2024) 120696, http://dx.doi.org/10.1016/j.renene.2024.120696.
[8] A. Mukherjee, A.S. Pujari, S.N. Shinde, U. Kashyap, L. Kumar, C. Subramaniam, S.K. Saha, Performance assessment of open thermochemical energy storage system for seasonal space heating in highly humid environment, Renew. Energy 201 (2022) 204–223, http://dx.doi.org/10.1016/j.renene.2022.10.075.
[9] J. Lin, Q. Zhao, H. Huang, H. Mao, Y. Liu, Y. Xiao, Applications of low-temperature thermochemical energy storage systems for salt hydrates based on material classification: A review, Sol. Energy 214 (2021) 149–178, http://dx.doi.org/10.1016/j.solener.2020.11.055.
[10] Y. Zhang, M. Hu, Z. Chen, Y. Su, S. Riffat, Exploring a novel tubular-type modular reactor for solar-driven thermochemical energy storage, Renew. Energy 221 (2024) 119767, http://dx.doi.org/10.1016/j.renene.2023.119767.
[11] W. Li, J.J. Klemeš, Q. Wang, M. Zeng, Salt hydrate–based gas-solid thermochemical energy storage: Current progress, challenges, and perspectives, Renew. Sustain. Energy Rev. 154 (2022) 111846, http://dx.doi.org/10.1016/j.rser.2021.111846.
[12] H. Liu, W. Wang, Y. Zhang, Performance gap between thermochemical energy storage systems based on salt hydrates and materials, J. Clean. Prod. 313 (2021) 127908, http://dx.doi.org/10.1016/j.jclepro.2021.127908.
[13] N. Mazur, H. Huinink, H. Fischer, O. Adan, A systematic deliquescent additive selection approach for enhancement of reaction kinetics of thermochemical heat storage materials, Sol. Energy Mater. Sol. Cells 263 (2023) 112588, http://dx.doi.org/10.1016/j.solmat.2023.112588.
[14] N. Yu, R. Wang, L. Wang, Sorption thermal storage for solar energy, Prog. Energy Combust. Sci. 39 (5) (2013) 489–514, http://dx.doi.org/10.1016/j.pecs.2013.05.004.
[15] K.E. N'Tsoukpoe, T. Schmidt, H.U. Rammelberg, B.A. Watts, W.K. Ruck, A systematic multi-step screening of numerous salt hydrates for low temperature thermochemical energy storage, Appl. Energy 124 (2014) 1–16, http://dx.doi.org/10.1016/j.apenergy.2014.02.053.
[16] K. Moulakhnif, H. Ait Ousaleh, S. Sair, Y. Bouhaj, A. El Majd, M. Ghazoui, A. Faik, A. El Bouari, Renewable approaches to building heat: Exploring cutting-edge innovations in thermochemical energy storage for building heating, Energy Build. 318 (2024) 114421, http://dx.doi.org/10.1016/j.enbuild.2024.114421.
[17] D. Mahon, P. Henshall, G. Claudio, P. Eames, Feasibility study of MgSO4 + zeolite based composite thermochemical energy stores charged by vacuum flat plate solar thermal collectors for seasonal thermal energy storage, Renew. Energy 145 (2020) 1799–1807, http://dx.doi.org/10.1016/j.renene.2019.05.135.
[18] W. Hua, H. Yan, X. Zhang, X. Xu, L. Zhang, Y. Shi, Review of salt hydrates-based thermochemical adsorption thermal storage technologies, J. Energy Storage 56 (2022) 106158, http://dx.doi.org/10.1016/j.est.2022.106158.
[19] Y.I. Aristov, Challenging offers of material science for adsorption heat transformation: A review, Appl. Therm. Eng. 50 (2) (2013) 1610–1618, http://dx.doi.org/10.1016/j.applthermaleng.2011.09.003.
[20] A. Frazzica, V. Brancato, A. Caprì, C. Cannilla, L. Gordeeva, Y. Aristov, Development of "salt in porous matrix" composites based on LiCl for sorption thermal energy storage, Energy 208 (2020) 118338, http://dx.doi.org/10.1016/j.energy.2020.118338.
[21] Y.-J. Huo, T. Yan, X.-L. Chang, H. Zhang, W.-G. Pan, Zeolite 13X/$MgSO_4$ as a potential heat storage material: Thermal performance characterization and sorption kinetics enhancement, New J. Chem. 47 (40) (2023) 18794–18802, http://dx.doi.org/10.1039/D3NJ03479H.
[22] J. Aarts, B. Van Ravensteijn, H. Fischer, O. Adan, H. Huinink, Polymeric stabilization of salt hydrates for thermochemical energy storage, Appl. Energy 341 (2023) 121068, http://dx.doi.org/10.1016/j.apenergy.2023.121068.
[23] W. Cai, W. Yang, Z. Jiang, F. He, K. Zhang, R. He, J. Wu, J. Fan, Numerical and experimental study of paraffin/expanded graphite phase change materials with an anisotropic model, Sol. Energy Mater. Sol. Cells 194 (2019) 111–120, http://dx.doi.org/10.1016/j.solmat.2019.02.006.
[24] N. Gao, L. Deng, J. Li, H. Huang, B. Zhou, Y. Zhou, Multi-form heat storage performance of expanded graphite based CaCl2 composites for low-grade heat source, Energy Rep. 8 (2022) 12117–12125, http://dx.doi.org/10.1016/j.egyr.2022.09.051.
[25] Q. Touloumet, L. Silvester, L. Bois, G. Postole, A. Auroux, Water sorption and heat storage in CaCl2 impregnated aluminium fumarate MOFs, Sol. Energy Mater. Sol. Cells 231 (2021) 111332, http://dx.doi.org/10.1016/j.solmat.2021.111332.
[26] A. Jabbari-Hichri, S. Bennici, A. Auroux, CaCl2-containing composites as thermochemical heat storage materials, Sol. Energy Mater. Sol. Cells 172 (2017) 177–185, http://dx.doi.org/10.1016/j.solmat.2017.07.037.
[27] B. Li, L. Buisson, R.-J. Clark, S. Ushak, M. Farid, A eutectic mixture of calcium chloride hexahydrate and bischofite with promising performance for thermochemical energy storage, Energies 17 (3) (2024) 578, http://dx.doi.org/10.3390/en17030578.
[28] S. Wei, W. Zhou, R. Han, J. Li, J. Gao, G. Zhao, Y. Qin, Scalable production of EP/CaCl2 @C multistage core–shell sorbent for solar-driven sorption heat storage application, Energy Fuels 35 (8) (2021) 6845–6857, http://dx.doi.org/10.1021/acs.energyfuels.0c04021.
[29] S. Wei, W. Zhou, R. Han, J. Gao, G. Zhao, Y. Qin, C. Wang, Influence of minerals with different porous structures on thermochemical heat storage performance of CaCl2-based composite sorbents, Sol. Energy Mater. Sol. Cells 243 (2022) 111769, http://dx.doi.org/10.1016/j.solmat.2022.111769.
[30] Y. Zhang, Z. Chen, C. Kutlu, Y. Su, S. Riffat, Investigation on a vermiculite-based solar thermochemical heat storage system for building applications, Futur. Cities Env. 8 (1) (2022) 8, http://dx.doi.org/10.5334/fce.153.
[31] B. Elahi, D. Salehzadeh, W.M.D. Vos, N. Shahidzadeh, G. Brem, M. Mehrali, Boosting stability of K2CO3 granules for thermochemical heat storage applications through innovative membrane encapsulation, Chem. Eng. J. 500 (2024) 157042, http://dx.doi.org/10.1016/j.cej.2024.157042.
[32] M. Gaeini, A.L. Rouws, J.W.O. Salari, H.A. Zondag, C.C.M. Rindt, Characterization of microencapsulated and impregnated porous host materials based on calcium chloride for thermochemical energy storage, Appl. Energy 212 (2018) 1165–1177, http://dx.doi.org/10.1016/j.apenergy.2017.12.131.
[33] D. Zou, X. Yue, T. He, J. Ding, D. Ba, Experimental research on the preparation of K2CO3/expanded vermiculite composite energy storage material, Materials 15 (10) (2022) 3702, http://dx.doi.org/10.3390/ma15103702.
[34] Z. Jiang, X. Li, Y. Jin, X. Zhang, L. Tong, L. Wang, Y. Ding, Particle technology in the formulation and fabrication of thermal energy storage materials, Chem. Ing. Tech. 95 (1–2) (2023) 40–58, http://dx.doi.org/10.1002/cite.202200113.
[35] J.X. Xu, T.X. Li, J.W. Chao, T.S. Yan, R.Z. Wang, High energy-density multi-form thermochemical energy storage based on multi-step sorption processes, Energy 185 (2019) 1131–1142, http://dx.doi.org/10.1016/j.energy.2019.07.076.
[36] Y. Zhang, Z. Chen, Y. Zhang, Y. Su, S. Riffat, Parameter control in synthesis of Vermiculite-CaCl2 composite materials for thermochemical adsorption heat storage, Energy 291 (2024) 130478, http://dx.doi.org/10.1016/j.energy.2024.130478.
[37] J. Reynolds, B. Abbas, G. Sullivan, J. Elvins, E. Jewell, J. Searle, L. Skevi, X. Ke, Optimisation of CaCl2 impregnated expanded graphite and alginate matrices – Targeted salt loading, Energy Convers. Manage. 302 (2024) 118145, http://dx.doi.org/10.1016/j.enconman.2024.118145.
[38] X. Liu, H. Wang, X. Liu, F. Yang, L. Guan, S. Sani, C. Sun, Y. Wu, Development of MgSO4 /mesoporous silica composites for thermochemical energy storage: The role of porous structure on water adsorption, Energy Rep. 8 (2022) 4913–4921, http://dx.doi.org/10.1016/j.egyr.2022.03.137.
[39] H. Wang, X. Liu, X. Liu, C. Sun, Y. Wu, Fluidisable mesoporous silica composites for thermochemical energy storage, Energy 275 (2023) 127255, http://dx.doi.org/10.1016/j.energy.2023.127255.
[40] B. Ding, C. Xu, Z. Liao, F. Ye, Study on long-term thermochemical thermal storage performance based on SrBr2-expanded vermiculite composite materials, J. Energy Storage 42 (2021) 103081, http://dx.doi.org/10.1016/j.est.2021.103081.
[41] S.P. Casey, J. Elvins, S. Riffat, A. Robinson, Salt impregnated desiccant matrices for 'open' thermochemical energy storage—Selection, synthesis and characterisation of candidate materials, Energy Build. 84 (2014) 412–425, http://dx.doi.org/10.1016/j.enbuild.2014.08.028.
[42] S. Columbu, M. Mulas, F. Mundula, R. Cioni, Strategies for helium pycnometry density measurements of welded ignimbritic rocks, Measurement 173 (2021) 108640, http://dx.doi.org/10.1016/j.measurement.2020.108640.
[43] L. Greenspan, Humidity fixed points of binary saturated aqueous solutions, J. Res. Natl. Bur. Stan. Sect. A 81A (1) (1977) 89, http://dx.doi.org/10.6028/jres.081A.011.
[44] F. Trausel, A.-J. De Jong, R. Cuypers, A review on the properties of salt hydrates for thermochemical storage, Energy Procedia 48 (2014) 447–452, http://dx.doi.org/10.1016/j.egypro.2014.02.053.
[45] Z. Cao, X. Cai, A.C. Feltrin, P. Feng, A. Kaiser, F. Akhtar, Calcium/strontium chloride impregnated zeolite A and X granules as optimized ammonia sorbents, RSC Adv. 12 (54) (2022) 34910–34917, http://dx.doi.org/10.1039/D2RA02981B.
[46] A.R. Sowunmi, C.O. Folayan, F.O. Anafi, O.A. Ajayi, N.O. Omisanya, D.O. Obada, D. Dodoo-Arhin, Dataset on the comparison of synthesized and commercial zeolites for potential solar adsorption refrigerating system, Data Brief 20 (2018) 90–95, http://dx.doi.org/10.1016/j.dib.2018.07.040.
[47] K.-M. Kim, H.-T. Oh, S.-J. Lim, K. Ho, Y. Park, C.-H. Lee, Adsorption equilibria of water vapor on zeolite 3A, zeolite 13X, and dealuminated Y zeolite, J. Chem. Eng. Data 61 (4) (2016) 1547–1554, http://dx.doi.org/10.1021/acs.jced.5b00927.
[48] X. Liu, X. Liu, F. Yang, Y. Wu, Experimental investigation of low-temperature fluidised bed thermochemical energy storage with salt-mesoporous silica composite materials, Appl. Energy 362 (2024) 122953, http://dx.doi.org/10.1016/j.apenergy.2024.122953.